

Marginally-Stable Thermal Equilibria of Rayleigh-Bénard Convection

Liam O'Connor¹, Daniel Lecoanet^{1,2}, and Evan Anders²

¹*Department of Engineering Sciences and Applied Mathematics,
Northwestern University, Evanston, IL 60208 USA and*

²*Center for Interdisciplinary Exploration and Research in Astrophysics,
Northwestern University, Evanston, IL, 60201 USA*

Natural convection is ubiquitous throughout the physical sciences and engineering, yet many of its important properties remain elusive—particularly in the large Rayleigh number regime. In this investigation, we derive and solve a quasilinear form of the Rayleigh-Bénard problem by representing the perturbations in terms of marginally stable eigenmodes. The amplitude of each eigenmode is determined by requiring that the background state maintains marginal stability. The background temperature profile evolves due to the advective flux of each eigenmode, as well as diffusion. The entire calculation is one-dimensional, and can be run on a workstation. We find the background temperature field evolves to an equilibrium state, where the advective flux from the marginally-stable eigenmodes and the diffusive flux sum to a constant. These marginally-stable thermal equilibria are exact solutions of the quasilinear equations. The mean temperature profile has thinner boundary layers and larger Nusselt numbers than thermally-equilibrated 2D and 3D simulations of the full nonlinear equations. We find the Nusselt number scales like $Nu \sim Ra^{1/3}$. When initializing a 2D simulation with a marginally-stable thermal equilibrium, we find the simulation does not exhibit the initial burst of turbulence typical of simulations initialized with the conductive background state plus noise. Although the Nu quickly equilibrates in these simulations, the kinetic energy evolves on a viscous timescale as domain-filling flywheel flows viscously attenuate.

I. INTRODUCTION

Rayleigh-Bénard convection plays a foundational role in astrophysical and geophysical settings. The resulting buoyancy-driven flows regulate heat transfer and generate large-scale vortices [1]. Turbulent convection, which is associated with large Rayleigh numbers Ra , is difficult to simulate. State of the art simulations performed by [2] have reached $Ra \sim 10^{14}$ but estimates for stars are $Ra \sim 10^{20}$ [3]. *put in a number for earth's interior?* The scaling behavior of the Nusselt number $Nu \sim Ra^\beta$ in the asymptotic ultimate regime is of particular interest. There exists a substantial body of work pertaining to this specific topic with no general consensus [4–10].

Absent solid evidence from direct numerical simulation, other methods have been developed to try to infer large- Ra behavior or otherwise gain insight. In the presence of other physical effects (e.g., rotation, magnetic fields), one can sometimes derive an asymptotically consistent set of reduced equations [11, 12]. Reduced models are potentially useful in this context because they may allow us to study the problem with less expensive computations. Another approach relates to unstable exact coherent states (ECS) [13–16]. Simulations and analysis performed by [17, 18] suggest that chaotic simulation trajectories can be represented by a Markov chain whose long-term behavior is given by the time-weighted-average over a finite set of unstable equilibria. Should that be the case, it is crucial that we discover and classify such equilibria.

Others have turned to studying quasilinear systems. The quasilinear approximation starts with a decomposition of all variables into a background and perturbations about this background. The approximation is to neglect

the influence of nonlinear interactions between the perturbations on the perturbations themselves [19]. This renders the perturbation equations linear. Although the quasilinear approximation greatly simplifies the problem, an additional condition must be imposed to determine the amplitude of the perturbations. In [20], researchers compute ECS in parallel shear flows by deriving and solving a quasilinear formulation of the Navier-Stokes equations via multi-scale asymptotic arguments. They assume the background velocity evolves on a slow timescale, and to determine the perturbation amplitudes they require marginal stability at each timestep. A similar strategy is employed by [21] to studying acoustic streaming. In that work, an analytic expression for the first-order perturbation's amplitude is found by deriving a solvability condition.

In this paper we solve the Rayleigh-Bénard convection problem using an analogous strategy. In section II we recall the underlying equations, and in section III we describe how we evolve the background temperature profile while maintaining marginal stability. Section IV describes the properties of the marginally-stable thermal equilibria, in particular how the Nusselt number and characteristic wavenumbers vary with the Rayleigh number. Finally, we describe the results of simulations initialized with marginally-stable thermal equilibria in section ??, and conclude in section VI.

II. MODEL SETUP

We begin with the non-dimensionalized Boussinesq approximation for Rayleigh-Bénard Convection. The domain \mathcal{D} is 2-dimensional, rectangular, and horizon-

tally periodic with spatial dimensions $0 < x < 4$ and $-1/2 < z < 1/2$. The fluid of interest is constrained between two flat boundaries at $z = -1/2$ and $z = 1/2$ with fixed temperatures 1 and 0 respectively. At both boundaries we specify impenetrable, no-slip conditions, such that the velocity $\mathbf{u} = u\hat{x} + w\hat{z} = \mathbf{0}$ at $z = \pm 1/2$, where \hat{x}, \hat{z} are the unit vectors in the x and z directions. The equations of motion are then given by

$$\nabla \cdot \mathbf{u} = 0 \quad (1)$$

$$\frac{\partial \mathbf{u}}{\partial t} + \mathbf{u} \cdot \nabla \mathbf{u} = -\nabla p + T\hat{z} + \mathcal{R}\nabla^2 \mathbf{u} \quad (2)$$

$$\frac{\partial T}{\partial t} + \mathbf{u} \cdot \nabla T = \mathcal{P}\nabla^2 T \quad (3)$$

where p is pressure and T is temperature. For completeness, we specify a final boundary condition $p = p_0$ at $z = \pm 1/2$. Any system of this form can be characterized by its dimensionless Rayleigh number $\text{Ra} = \frac{g\alpha L^3 \Delta T}{\nu \kappa}$ and Prandtl number $\text{Pr} = \frac{\nu}{\kappa}$, where $g, \alpha, L, \Delta T, \nu, \kappa$ are the gravitational acceleration, coefficient of thermal expansion, domain height, opposed temperature difference, kinematic viscosity, and thermal diffusivity respectively. For convenience, we define

$$\mathcal{R} = \sqrt{\frac{\text{Pr}}{\text{Ra}}}, \quad \mathcal{P} = \frac{1}{\sqrt{\text{Pr Ra}}}. \quad (4)$$

To derive the quasilinear form, we posit that an arbitrary field f can be represented as the sum of a mean profile (denoted by \bar{f}) and a perturbation function (denoted by f').

$$\mathbf{u}(x, z, t) = \mathbf{u}'(x, z, t) \quad (5)$$

$$= u'(x, z, t)\hat{x} + w'(x, z, t)\hat{z} \quad (6)$$

$$T(x, z, t) = \bar{T}(z, t) + T'(x, z, t) \quad (7)$$

$$p(x, z, t) = \bar{p}(z, t) + p'(x, z, t). \quad (8)$$

where the mean-velocity components vanish due to incompressibility and symmetry. Perturbations are defined to have no horizontal-average

$$\langle f'(x, z, t) \rangle_x \equiv \int_0^4 f'(x, z, t) dx = 0. \quad (9)$$

Substituting (7) into (3) and taking the horizontal-average reduces the system to a simple initial value problem (IVP) for \bar{T}

$$\frac{\partial \bar{T}}{\partial t} + \langle w'T' \rangle_x = \mathcal{P} \frac{\partial^2 \bar{T}}{\partial z^2}, \quad (10)$$

with associated boundary conditions $\bar{T}(-1/2, t) = 1$ and $\bar{T}(1/2, t) = 0$. It should be noted that we could obtain a similar IVP for u by breaking symmetry and considering some nontrivial mean horizontal flow $\bar{u}(z, t)$. However we must have $\bar{w}(z, t) = 0$ due to incompressibility.

To solve (10) numerically, we need an expression for the perturbation so we can calculate the advective heat

flux. Here we will make the quasilinear approximation, dropping the $\mathbf{u}' \cdot \nabla \mathbf{u}'$ and $\mathbf{u}' \cdot \nabla T'$ terms from the evolution equations for the perturbations. Substituting (5)–(8) into (1)–(3) and subtracting (10) from the resulting temperature equation, and linearizing gives

$$\nabla \cdot \mathbf{u}' = 0 \quad (11)$$

$$\frac{\partial \mathbf{u}'}{\partial t} = -\nabla p' + T'\hat{z} + \mathcal{R}\nabla^2 \mathbf{u}' \quad (12)$$

$$\frac{\partial T'}{\partial t} + \frac{\partial \bar{T}}{\partial z} w' = \mathcal{P}\nabla^2 T' \quad (13)$$

with Dirichlet boundary conditions

$$T'|_{z=\pm 1/2} = 0, \quad u'|_{z=\pm 1/2} = 0, \quad p'|_{z=\pm 1/2} = 0. \quad (14)$$

This is now a linear problem in \mathbf{u}' and T' which can be solved as an eigenvalue problem.

In his groundbreaking report [22], Lord Rayleigh observed that (11)–(13) can be manipulated into a separable form with generalized solutions

$$w'(x, z, t) = A \Re \left[W(z) e^{i(k_x x - st)} \right], \quad (15)$$

$$u'(x, z, t) = A \Re \left[U(z) e^{i(k_x x - st)} \right], \quad (16)$$

$$T'(x, z, t) = A \Re \left[\theta(z) e^{i(k_x x - st)} \right], \quad (17)$$

$$p'(x, z, t) = A \Re \left[P(z) e^{i(k_x x - st)} \right], \quad (18)$$

where A is the (undetermined) mode amplitude, $s = \sigma + i\omega$ and k_x is constrained, by periodicity, to the countably infinite set (spectrum) of wavenumbers

$$k_x \in \left\{ \frac{n\pi}{2} \mid n \in \mathbb{N} \right\}. \quad (19)$$

We normalize the eigenmodes to have

$$\langle |\theta|^2 \rangle_{\mathcal{D}} = 1. \quad (20)$$

For each k_x , we can assess the stability of the perturbations by solving for the eigenvalue s , whose imaginary component ω plays the role of an exponential growth rate. Solution yields a finite set of eigenvalues, among which, that with maximum ω is assumed to be dominant ***I don't understand this sentence***. Positive eigenvalues indicate that the system is unstable to small disturbances of wavenumber k_x , while negative eigenvalues indicate stability. A complete linear stability analysis requires solution over the full spectrum of wavenumbers. The prototypical case is used to demonstrate that the critical Rayleigh number $\text{Ra}_c = 1708$ when $\frac{\partial \bar{T}}{\partial z} = -1$.

To calculate the advective heat flux in equation 10, we can sum $\langle w'T' \rangle_x$ from each horizontal wavenumber individually. In this way, the heat flux from the perturbations influence the evolution of \bar{T} . But the evolution of \bar{T} also influences the perturbations, as equation 13 depends on $\partial_z \bar{T}$. Thus, the mean temperature and perturbations fields are coupled.

III. PERTURBATION EVOLUTION

The linearized system (11)–(13) cannot determine the amplitude of the eigenmodes, A . However, the advective heat flux is proportional to A^2 , so we need to specify the amplitude in order to solve equation 10. To evolve \bar{T} , we assume the perturbations evolve on a much faster timescale than the mean temperature, as in [21]. Stable modes decay away rapidly. Unstable modes will not persist on the slow timescale because the advective term $\langle w'T' \rangle_x$ tends to stabilize \bar{T} , thereby creating a negative feedback loop. Only marginally stable modes can be maintained on the slow timescale. Therefore the amplitude A must satisfy

$$\max_{k_x} \{\omega\} = 0. \quad (21)$$

For various Ra and fixed $Pr = 1$, we seek marginally-stable thermal equilibria (MSTE) satisfying $\frac{\partial \bar{T}}{\partial t} = 0$ according to . We employ the **Dedalus** pseudo-spectral python framework [23] to solve the EVP outlined in Section II as well as the IVP (10) by representing each field with Chebyshev polynomials. We use the 3/2 dealiasing rule to calculate the advective heat flux. The necessary number of basis functions varies, as eigenfunctions and temperature profiles associated with large Ra admit increasingly small-scale features. We use the **Eigentools** package to manipulate the eigenfunctions and calculate the advective heat flux $\langle w'T' \rangle_x$ *cite eigentools*.

At $t = 0$, we begin with a marginally-stable initial profile $\bar{T}(z, 0)$ whose construction is outlined in appendix A. At some arbitrary time $t = t_0$, we seek to evolve $\bar{T}(z, t_0)$ into a new marginally-stable profile $\bar{T}(z, t_0 + \Delta t)$ according to (10), using backward Euler to evolve the diffusion term and forward Euler to evolve the advection term. This requires us to determine the amplitude of the eigenfunction A . We will now illustrate our method of finding A^2 through an example.

An iteration is performed as follows. Consider a marginally-stable temperature profile $\bar{T}(z, t_0)$. By definition, its maximum eigenvalue is 0. Diffusing $\bar{T}(z, t_0)$ tends to increase its eigenvalues. Ignoring the diffusive term and evolving according to advection tends to stabilize the system. The appropriate amplitude A^2 can then be approximated by

$$A^2 \approx -\frac{\omega_{\text{diff}}}{\omega_{\text{adv}}} \quad (22)$$

where ω_{diff} and ω_{adv} refer to the diffused and advected eigenvalues of the initially marginal mode. We illustrate these trends in Figure 1. $\bar{T}(z, t)$ is then evolved according to (10) and another eigenvalue solve is performed. Given a fixed timestep Δt , we assume the dominant eigenvalue can be described by a continuous function $\omega_{\text{max}}(A^2)$ which is locally differentiable. We use Newton's method to find an amplitude which satisfies our marginal stability tolerance criterion *what is the criterion?*. Crucially, we do not assume the k_x of the marginally-stable is fixed.

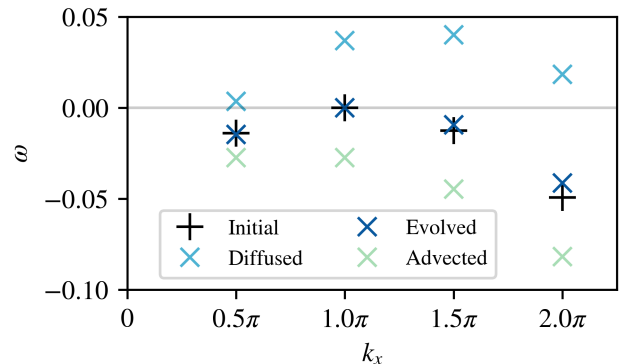


FIG. 1. Eigenvalue spectra for $Ra = 10^5$. The spectrum of an “initial” marginally-stable mean temperature profile $\bar{T}(z, t_0)$ has a maximum eigenvalue of 0. Given a small fixed timestep Δt , diffusion destabilizes the system, increasing its eigenvalues. Advection tends to stabilize the system, decreasing its eigenvalues. We find the eigenfunction amplitude A^2 such that the combination of diffusion and advection yields a new, “evolved,” marginally-stable mean temperature profile $\bar{T}(z, t_0 + \Delta t)$.

In section III A we specify procedures for the treatment of multiple simultaneously marginal modes.

A. Treatment of multiple marginally-stable modes

In most cases, we eventually encounter eigenvalue spectra with multiple simultaneously marginal modes. If ignored, we are forced to reduce the timestep and allow the modes to alternate which is marginally stable. Instead, we generalize the advective term in (10) to accommodate N simultaneously marginal modes

$$\langle w'T' \rangle_x = \sum_{n=1}^N 4A_n^2 \int \Re [W_n \theta_n^*] dz \quad (23)$$

where W_n and θ_n are the eigenmodes associated with $k_x = \frac{n\pi}{2}$. There are now N amplitudes to solve for and N eigenvalues to keep marginally-stable. In general, we expect a function $\omega : \mathbb{R}^N \rightarrow \mathbb{R}^N$ to have isolated roots (should they exist). We employ Broyden's method for root-finding in multi-dimensional functions whose derivatives are not explicitly known *Should describe this better... don't you calculate the Jacobian, invert it, and then refine the roots using Broyden's method?*. Difficulty arises when transitioning between different numbers of marginal modes. *Should describe what happens when you add modes* Here we rely on $A^2 > 0$ by asserting that a mode which is *close enough* to marginal-stability can be included in the iteration provided that its respective amplitude is positive *this is a description of how you remove modes, but it is a bit confusing*. Should we converge upon a negative

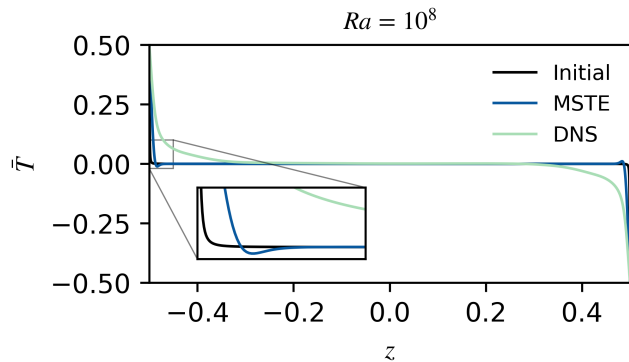


FIG. 2. Mean temperature profiles \bar{T} for $Ra = 10^8$. The initial profile is given by (A1). MSTE refers to the mean temperature profile of the marginally-stable thermally-equilibrated state. DNS was obtained by performing a 2D nonlinear simulation of (1)–(3) with *Dedalus* until thermal and kinetic relaxation. DNS temperature data are horizontally- and time-averaged. The initial, MSTE, and DNS profiles have increasingly relaxed boundary regions respectively. The MSTE profile exhibits prominent dips, nested alongside the boundary regions. The source of this feature is not well understood, but similar temperature gradient reversal regions were found by [16] along the midlines of 2D convective cellular solutions at $Ra \sim 10^6$.

amplitude, that mode is discarded and the iteration is repeated.

IV. PROPERTIES OF THERMALLY EQUILIBRATED STATES

We evolve \bar{T} as described above until $\partial_t \bar{T} \approx 0$ *what is your criterion for equilibrium?* In this marginally-stable thermal equilibrium, \bar{T} does not evolve in time, and the perturbations also do not evolve in time, as they are marginally stable. Thus, these configurations are exact solutions to the quasilinear equations (equations 10–13). They differ from the usual ECS in that ECS are fixed points of the full nonlinear problem (1)–(3). Such definitions are not mutually exclusive, but in general we can assume that MSTE and ECS are not steady with respect to their counterparts' equations. We compute symmetric MSTE for Ra in the range $10^5 - 10^9$ *Some-where you need to state we impose symmetry on the temperature field... this should go in section 3.*

Figure 2 gives temperature profiles for $Ra = 10^8$ where the initial profile, whose construction is outlined in A, is employed at iteration 0. DNS (direct numerical simulations) are performed by solving (1)–(3) with *Dedalus*, followed by horizontal- and time- averaging. The DNS curve is more diffuse than the MSTE curve, which in turn, is more diffuse than the initial curve. Performing an eigenvalue solve by setting \bar{T} equal to the DNS profile yields positive eigenvalues. This suggests that MSTE

might maximize boundary layer thickness, while subject to the marginal stability constraint.

The most resilient and unexpected feature of MSTE temperature profiles are the pronounced dips adjacent to the boundary layers. These dips appear in every solution, regardless of Ra . Physically, they correspond to thin layers in which the mean temperature gradient reverses, contradicting an important hypothesis of [4, 5]. This counter-diffusion, which opposes overall heat transfer, is overcome by the coinciding advective flux, shown in Figure 3. We don't understand the source of these dips, but similar temperature gradient reversals were reported by [16] along the midlines of 2D convective cellular solutions at $Ra \sim 10^6$.

Equilibrated states exhibit distinct behaviors for large and small Ra . This contrast is illustrated in Figure 3, where we give heat flux profiles and eigenvalue spectra for two cases: $Ra = 2 \times 10^5$ and $Ra = 10^9$. For $Ra = 2 \times 10^5$, there is a single marginal mode at $k_x = 1.5\pi$ whose advection occupies the bulk of the domain. These states have relaxed boundary layers which gradually subside as advection becomes the dominant flux component. Such transitional regions do not appear for $Ra = 10^9$. In this case the shift from diffusion to advection is sharp. Thin advection profiles, belonging to high-wavenumber modes, hug the boundary layer. Closer to the bulk of the domain, we see wider advection profiles corresponding to modes in the second marginal group $k_x = 6\pi, 6.5\pi$. The $k_x = 1.5\pi$ mode forms the large-scale convective cell structures observed in DNS, again occupying the bulk of the domain.

MSTE of large Ra tend to have a diverse combination of marginal modes. In every case, the $k_x = 1.5\pi$ mode is included and is often unaccompanied by adjacent modes. In Figure 4 we give the wavenumbers k_x of marginal modes. These wavenumbers often appear in adjacent pairs, where the larger mode is denoted with an x and the smaller with a +. For $Ra \geq 10^6$, a second branch of marginal modes is introduced as shown in light green, obeying some power-law with respect to Ra . For large Ra , the advectons of this maximum branch opposes the strong diffusion of the thin MSTE boundary layers. At $Ra \geq 10^8$, a third branch appears (shown in light blue), splitting the widening gap between the other two. This development is associated with moderately wide advection profiles, filling a niche in the total flux by uniting the thin profiles of the maximum branch with those of the bulk-domain-oriented minimum branch.

The largest marginal wavenumber $\max\{k_x\}$ (represented by the light green branch in Figure 4) serves as an inverse minimum length-scale in the x direction. The finest structures in $\bar{T}(z)$ appear near the boundaries, requiring more basis functions (resolution) at large Ra . Naturally, this provides a complementary minimum length-scale for z . We define the interior boundary layer threshold as the z -coordinate at which $\frac{\partial \bar{T}}{\partial z} = 0$. In Figure 5, we illustrate the constant ratio between these two quantities for various Ra . We can assume from this length scale agreement that the mean-squared x and z

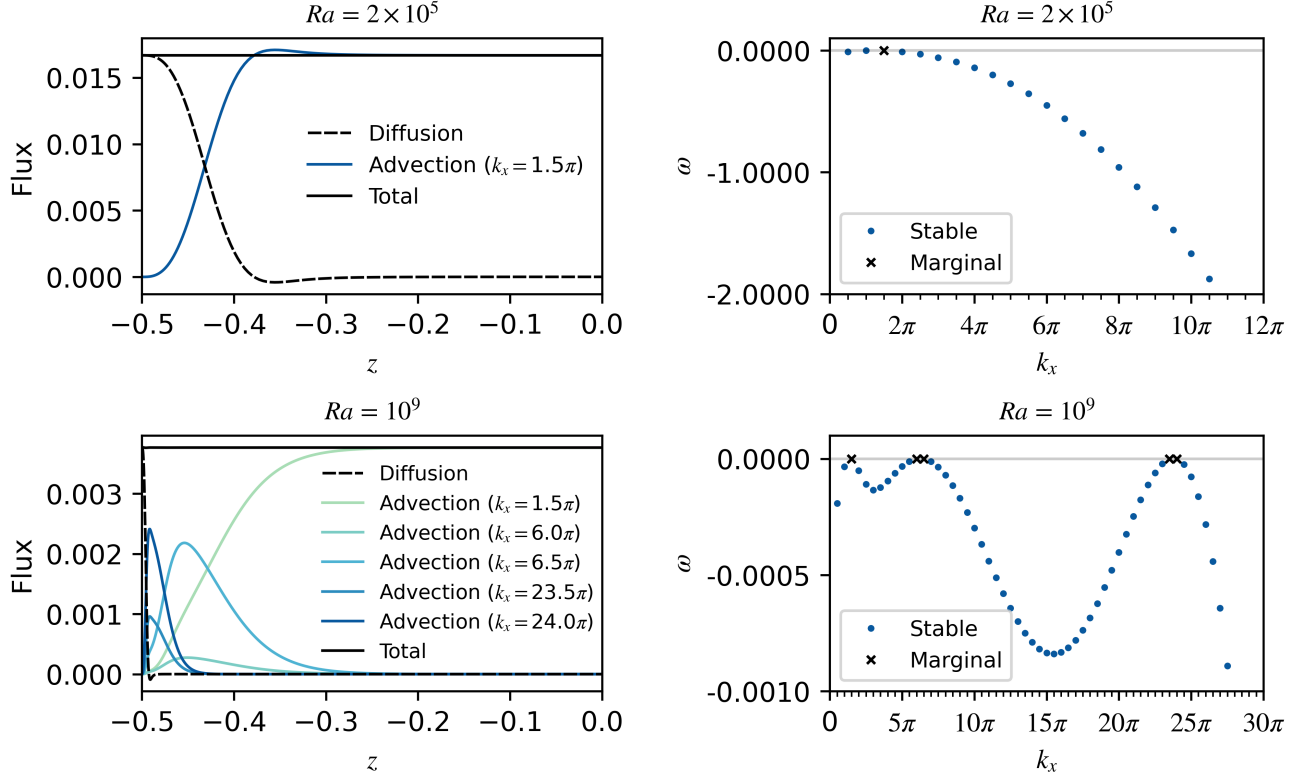


FIG. 3. Heat fluxes (left) and eigenvalue spectra (right) of equilibrated states $Ra = 2 \times 10^5$ (top) and $Ra = 10^9$ (bottom). Advection profiles belong to marginally-stable modes. For low Ra , a single mode with $k_x = 1.5\pi$ is sufficient to oppose boundary layer diffusion and facilitate heat flux throughout the bulk of the domain. For large Ra , high-wavenumber modes contribute pronounced small-scale advection profiles which tightly hug the thin boundary layers. A combination of progressively wider advection profiles is necessary to transition to the $k_x = 1.5\pi$ mode.

components of the temperature and velocity gradients are proportional for various Ra

$$\begin{aligned} \left\langle \frac{\partial T}{\partial x} \cdot \frac{\partial T}{\partial x} \right\rangle_{\mathcal{D}} &\propto \left\langle \frac{\partial T}{\partial z} \cdot \frac{\partial T}{\partial z} \right\rangle_{\mathcal{D}} \\ \left\langle \frac{\partial \mathbf{u}}{\partial x} \cdot \frac{\partial \mathbf{u}}{\partial x} \right\rangle_{\mathcal{D}} &\propto \left\langle \frac{\partial \mathbf{u}}{\partial z} \cdot \frac{\partial \mathbf{u}}{\partial z} \right\rangle_{\mathcal{D}}. \end{aligned}$$

This is consistent with the mean squared gradient assumptions of [4]. The quasilinear model cannot describe arbitrarily small scale structures. This is a consequence of us collapsing the problem into a single dimension via mode-discretization.

In general, MSTE can be characterized by their boundary layer height, from which, the rest of their properties follow. In Figure 6, we illustrate the scaling behavior of the boundary layer height $\delta = Ra^{-1/3}$. This is consistent with Malkus' classical marginal-stability theory, a scaling argument which perceives the boundary regions as subdomains which are themselves marginally-stable [4].

The Nusselt number, which measures convective performance is given by

$$Nu = \frac{\langle A^2 \langle w' T' \rangle_x - \mathcal{P} \frac{\partial \bar{T}}{\partial z} \rangle_z}{\langle -\mathcal{P} \frac{\partial \bar{T}}{\partial z} \rangle_z}.$$

I'm giving the full Nu definition here so it's clear what's reported later in the simulations. There is no general consensus surrounding the scaling behavior of Nu for high Ra systems, which are of particular importance in astrophysical and geophysical systems. In Figure 7 we report Nu for MSTE, "steady rolls" ECS [15], and DNS [24, 25]. All states obey $Nu \sim Ra^\beta$ with classical scaling $\beta = 1/3$ in the ECS and MSTE. [15] hypothesized that the Nu of all ECS which admit classical Malkus scaling must always exceed the Nu of turbulent convection. If we generalize this notion to include quasilinear equilibria, our findings agree; MSTE have larger Nu than 2D and 3D DNS. This might be due to the chaotic transitions among the unstable periodic orbits outlined by [17, 18] inhibiting heat flux. We might also anticipate the existence of similar equilibria with smaller Nu , occupying complementary nodes in the Markov chain whose behavior agrees with DNS.

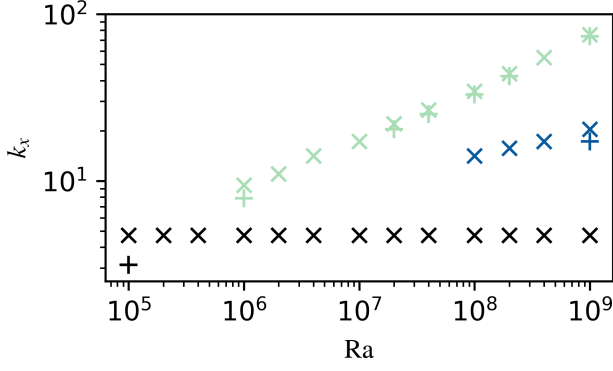


FIG. 4. Wavenumbers of marginally-stable modes of thermally equilibrated states. Marginal modes often appear in adjacent pairs, which we denote with a common color. For example, the spectrum corresponding to $Ra = 10^5$ has adjacent marginal wavenumbers $k_x = \pi, 1.5\pi$. The $Ra = 10^9$ spectrum, shown in lower right corner of Figure 3, has three groups of maxima, with a single marginal mode in the first group ($k_x = 1.5\pi$), two adjacent marginal modes in the second group ($k_x = 6\pi, 6.5\pi$), and two adjacent marginal modes in the third group ($k_x = 23.5\pi, 24\pi$). The largest wavenumbers of the green branch obey a power-law relationship with Ra

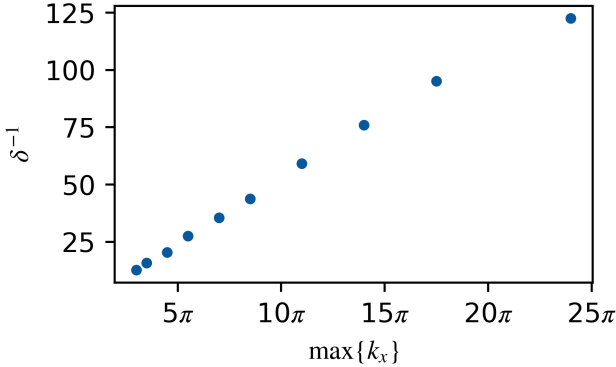


FIG. 5. For $Ra \geq 10^6$, the maximum marginally-stable wavenumbers (corresponding to the green x markers in Figure 4) are inversely related to the boundary layer heights δ . $(\max\{k_x\})^{-1}$ gives a minimum x length scale for the perturbations, and consequently, the advection. For large Ra , the boundary layers admit small scale features, requiring more basis functions (higher resolution). It follows that the minimum z length scale to agrees with the boundary layer height δ . This suggests that the minimum x and z length scales obey some constant ratio over various Ra .

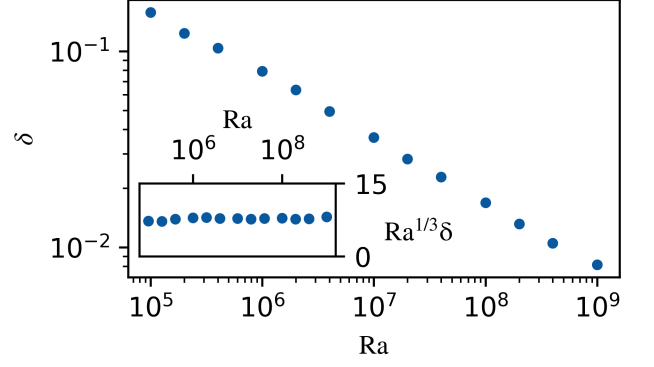


FIG. 6. Boundary layer height δ of MSTE. We define the threshold of each boundary layer as the z -coordinate at which $\frac{\partial T}{\partial z} = 0$, corresponding to the local extrema of the MSTE curve in Figure 2. Plotting on a log-log scale, we find that δ and Ra obey a power-law relationship. We also demonstrate that $Ra^{1/3}\delta$ is approximately constant with respect to Ra which is consistent with [4]

V. SIMULATIONS WITH THERMALLY EQUILIBRATED INITIAL CONDITIONS

This investigation is partially motivated by the prospect of decreasing DNS times by employing MSTE as initial conditions. Conventionally, (1)–(3) are solved via DNS with the linear initial conditions

$$\begin{aligned} T(x, z)|_{t=0} &= 0.5 - z \\ \mathbf{u}(x, z)|_{t=0} &= \mathbf{0} \\ p(x, z)|_{t=0} &= 0 \end{aligned} \quad (24)$$

where t in this section now refers to the simulation time as opposed to the thermal equilibration time used previously. We define the MSTE initial conditions ***This needs to be updated***

$$\begin{aligned} T(x, z)|_{t=0} &= \bar{T}(z) + \sqrt{2} \sum_{n=1}^N A_n \operatorname{Re} \left[\theta_n(z) e^{ik_{x_n} x} \right] \\ \mathbf{u}(x, z)|_{t=0} &= \sqrt{2} \sum_{n=1}^N A_n \operatorname{Re} \left[\left(U_n(z) \hat{x} + W_n(z) \hat{z} \right) e^{ik_{x_n} x} \right] \\ p(x, z)|_{t=0} &= \sqrt{2} \sum_{n=1}^N A_n \operatorname{Re} \left[P_n(z) e^{ik_{x_n} x} \right] \end{aligned} \quad (25)$$

where $\theta_n(z), U_n(z), W_n(z), P_n(z); A_n$; and k_{x_n} refer to the complex eigenfunctions, amplitude, and wavenumber at the n th marginal mode respectively. The $\sqrt{2}$ factor is necessary for eigenfunction normalization.

Simulations with MSTE initial conditions do not exhibit a convective-transient period, as the large-scale anatomy of convective cells exists on initialization. This is illustrated in Figure 8, where the sharp spike in Nu

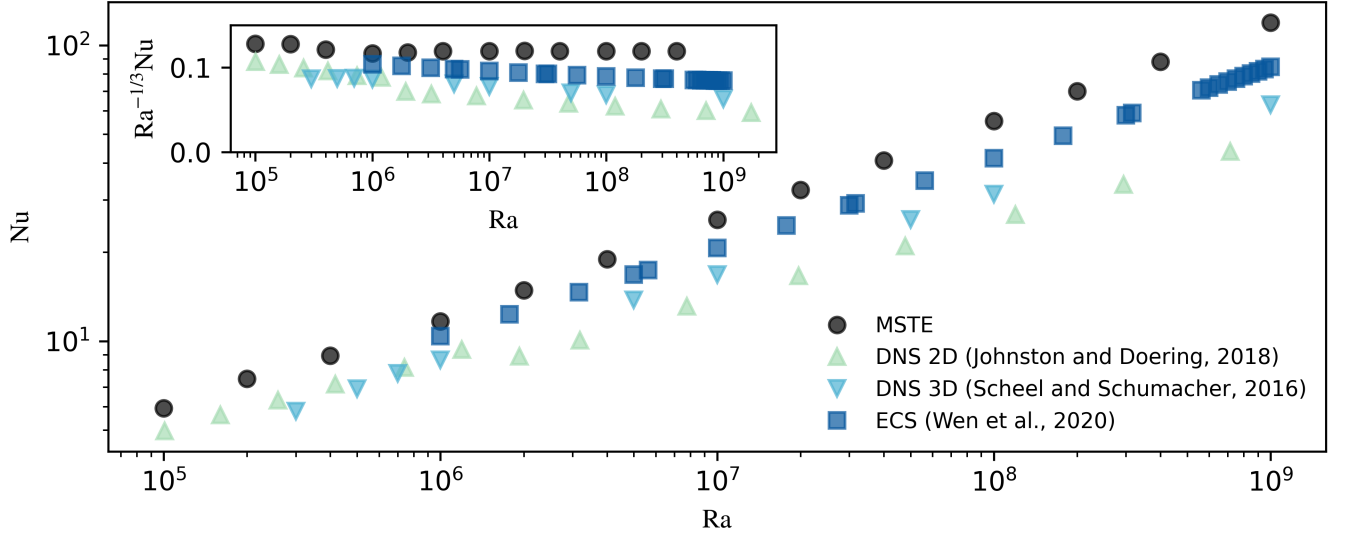


FIG. 7. Nusselt numbers are shown for MSTE, aspect-ratio-optimized “steady rolls” ECS [15], as well as statistically-steady 2D and 3D DNS [24, 25]. All datasets obey power-law relationships, with the MSTE and ECS scaling like $Nu \sim Ra^{1/3}$. MSTE have greater Nu than the ECS, which in turn, have greater Nu than the DNS. This can be explained by the contrasting boundary layer geometries shown in Figure 2.

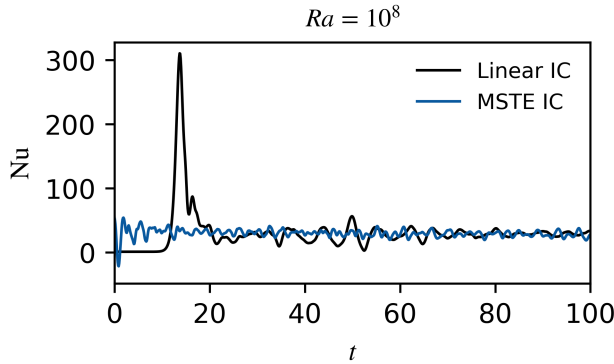


FIG. 8. Nusselt numbers of simulations performed at $Ra = 10^8$ with the conventional initial conditions (black) and MSTE initial conditions (blue). MSTE simulations do not undergo a convective-transient period because the characteristic large-scale convective cell structure exists on initialization.

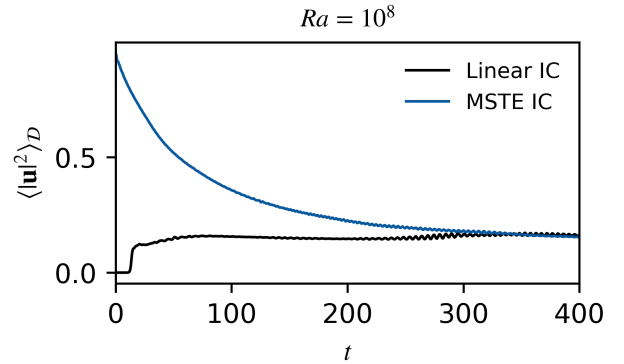


FIG. 9. Average kinetic energies are reported for the same simulations illustrated in Figure 8 ($Ra = 10^8$). The eigenfunctions belonging to MSTE have significantly more kinetic energy than the statistically-steady state. Kinetic equilibrium is achieved on the viscous time-scale $t_\nu \sim \sqrt{Ra/Pr}$.

is associated with a turbulent transitional period of upwelling until the distinctive flywheel structure is established. Simulation of this transitional period is prohibitive [26]. For high Ra experiments, researchers often “bootstrap” data by initializing simulations with the results of similar Ra runs [24, 27]. MSTE can be perceived as a set of initial conditions, designed for avoiding the simulation of transitional high Reynolds number flows.

MSTE are laminar, lacking the small-scale structures associated with moderate to high Ra experiments. This is an apparent consequence of the quasilinear assumptions. If we perceive MSTE as background states, DNS

suggest that plumes, vortex sheets, and other unstable turbulent features inhibit total heat transfer. This perspective agrees with conventional models of transitions to turbulent flows, such as Boussinesq’s turbulent-viscosity hypothesis [28]. The emergence of small-scale velocity structures tends to increase total shear [29–31], thereby impeding buoyancy-driven flows and decreasing advection in the bulk of the domain. We could also attribute the diffuse DNS temperature profile in Figure 2 with unsteady boundary-layer penetration and mixing that MSTE do not exhibit.

The average kinetic energies of MSTE are significantly

larger than those of the statistically-steady state, as shown Figure 9. This is postpones kinetic relaxation because the large-scale flows decay on a viscous time-scale

$$t_\nu \sim \sqrt{\frac{\text{Ra}}{\text{Pr}}}.$$

Consequently, MSTE initial conditions do not reduce the simulation time required to achieve a statistically-steady state – instead they increase it considerably. This suggests the MSTE background state perspective is partially flawed, as an appropriate background state would approximate $\langle |\mathbf{u}|^2 \rangle_{\mathcal{D}}$ with more fidelity.

VI. DISCUSSION

In general, the reduced model we study in this paper can be perceived as a unique way to describe Rayleigh–Bénard convection. To compute MSTE, we construct a marginally-stable mean temperature profile and evolved it according to its eigenfunctions’ advection and its own diffusion. We assume that stable and unstable modes cannot persist over a long time scale. The marginal stability constraint then fixes the unknown ratio between advection and diffusion (eigenfunction amplitude A^2). We use standard root-finding algorithms to solve for the appropriate A^2 at each iteration, until, the fixed combination of diffusion and advection sum to a constant flux.

Solutions retain several key features that are prevalent in experiments and simulations: $\text{Nu} \sim \text{Ra}^{1/3}$ scaling, large-scale convective cell structures, and minimum length scale agreement. They also exhibit unique and unexpected features: mean temperature gradient-reversals/dips, high kinetic energy flows, and greater Nu than other time-invariant solutions. We obtain indistinguishable solutions despite initializing with various mean temperature profiles $T(z, 0)$. Thus solutions might be unique, but we cannot demonstrate this rigorously.

Simulations performed with MSTE initial conditions (25) do not undergo an early convective transient period, but have faster flows and greater Nu when compared with DNS. From a dynamical systems perspective, unstable orbits depart from MSTE and approach the global attractor on a viscous time-scale *Still reading about this*. This requires more CPU-hr to achieve relaxation when compared to the conventional linear initial condition (24).

As previously noted, solving the EVP for statistically-steady DNS data yields positive eigenvalues; the system is in a perpetual state of instability. Unstable modes tend to stabilize the system rapidly, creating a negative feedback loop whose average state is linearly unstable. We might curtail the disagreement between MSTE and DNS adjusting our marginal-stability criterion. Should the time scales not be entirely separate, we might anticipate the long-term persistence of moderately unstable

modes. Such an instability cannot be described by our model independently (we do not know, a priori, *how unstable* the equilibria should be) but it might prove fruitful to investigate moderately unstable thermal equilibria (MUTE). More precisely, instead of traversing the manifold of marginally-stable states toward MSTE, we could consider the manifold of states whose maximum eigenvalue(s) ω_{\max} agree with some other stability constraint. Note that under this definition, ECS are themselves MUTE, because they are thermally-equilibrated and generally unstable, though they need not satisfy the quasilinear form.

We cannot use our reduced quasilinear model to predict $\text{Nu} \sim \text{Ra}^\beta$ for large Ra without some complementary stability constraint. The eigenvalues of DNS data might provide an informative stability constraint (we could find MUTE and compare them with DNS data), but this would be self-defeating in general. Instead we seek to combine reduced models to approximate β without DNS. Under the marginal-stability constraint, we found that MSTE exhibit classical Malkus scaling, having marginally-stable boundary layers. We could instead require that the eigenvalues of MUTE agree with the eigenvalues of the analytic 1D boundary layer predictions of [32, 33] (which remain in development), allowing us to refine and expand these estimates into 2D MUTE. The process for finding such MUTE would not involve DNS. Equilibria would satisfy only the quasilinear problem and stability constraint. They ought to agree with DNS data more than MSTE, ideally having slower flows. This is reasonable to expect because accurate boundary layer approximations and DNS data should have similar stability characteristics. We also observed that MSTE have marginally stable boundary layers, so it would be reasonable to place a hypothetical stability constraint on MUTE based on boundary layer approximations. By definition, MUTE are unstable and would likely admit more diffuse boundary layer structures, requiring smaller $A^2(t)$ (less advection) to satisfy the stability constraint and thereby reducing Nu, $\langle |\mathbf{u}|^2 \rangle_{\mathcal{D}}$ and possibly β .

ACKNOWLEDGMENTS

The authors thank Geoff Vasil, Greg Chini, and Emma Kaufman for their valuable feedback and suggestions. We also thank the *Dedalus* and *Eigentools* development teams. Computations were performed on the NASA Pleiades system.

Appendix A: Initial buoyancy profile

We initialize the thermal-equilibration algorithm with [32]’s analytical thermal boundary layer equation for tur-

bulent Rayleigh-Bénard convection, given by

$$\bar{T}_0(\xi) = \frac{\sqrt{3}}{4\pi} \log \frac{(1+a\xi)^3}{1+(a\xi)^3} + \frac{3}{2\pi} \arctan \left(\frac{4\pi}{9} \xi - \frac{1}{\sqrt{3}} \right) + \frac{1}{4}$$

$$\xi = \frac{z}{\delta_0}, \quad a = \frac{2\pi}{3\sqrt{3}} \quad (\text{A1})$$

where δ_0 is the boundary layer height. We expect that each Ra is associated with a unique δ_0 for which $\bar{T}_0(z)$ is marginally-stable. It should be noted that when experimenting with various initial profiles (tanh, erf, etc.), we obtain indistinguishable equilibrated states, implying that solutions may be unique. An example of (A1) is given by the blue curve in Figure 2.

1. MSTE Metrics

Ra	Pr	$k = 2\pi/\Gamma$	$N_x \times N_z$	Nu	Re
$10^{13/4}$	1	π	128×65	1.056590	1.617336
1.9×10^3	1	π	128×65	1.145807	2.682155
2×10^3	1	π	128×65	1.212037	3.317190
2.25×10^3	1	π	128×65	1.355410	4.550975
2.5×10^3	1	π	128×65	1.474455	5.537770
2.75×10^3	1	π	128×65	1.575599	6.391812
3×10^3	1	π	128×65	1.663162	7.159844
$10^{14/4}$	1	π	128×65	1.714193	7.624400
3.5×10^3	1	π	128×65	1.808754	8.526064
4×10^3	1	π	128×65	1.926775	9.740578
4.5×10^3	1	π	128×65	2.025985	10.85141
5×10^3	1	π	128×65	2.111714	11.88534
$10^{15/4}$	1	π	128×65	2.204811	13.09152
8×10^3	1	π	128×65	2.476330	17.05494
10^4	1	π	128×65	2.648664	20.07400
$10^{17/4}$	1	π	128×65	3.122843	29.50047
$10^{18/4}$	1	π	128×65	3.665041	42.29585
$10^{19/4}$	1	π	128×65	4.287042	59.56858
10^5	1	π	128×65	4.994322	82.84462
$10^{21/4}$	1	π	128×65	5.795869	114.2355
$10^{22/4}$	1	π	128×97	6.703915	156.5252
$10^{23/4}$	1	π	128×97	7.732236	213.4031
10^6	1	π	128×97	8.896615	289.7982
$10^{25/4}$	1	π	256×97	10.21546	392.2837
$10^{26/4}$	1	π	256×129	11.71065	529.6372
$10^{27/4}$	1	π	256×129	13.40898	713.6005
10^7	1	π	512×129	15.34493	959.9367
1.35×10^7	1	π	512×129	16.46456	1119.932
1.5×10^7	1	π	512×129	16.87881	1182.172
1.6×10^7	1	π	512×193	17.13944	1222.005
1.65×10^7	1	π	512×193	17.26636	1241.484
1.7×10^7	1	π	512×193	17.39216	1260.709
1.736×10^7	1	π	512×193	17.48282	1274.414
1.76×10^7	1	π	512×193	17.54351	1283.493
$10^{29/4}$	1	π	512×193	17.58987	1290.377
1.786×10^7	1	π	512×193	17.60946	1293.277
1.8×10^7	1	π	512×193	17.64500	1298.522
1.85×10^7	1	π	512×193	17.77160	1317.122
1.9×10^7	1	π	512×193	17.89693	1335.501
1.95×10^7	1	π	512×193	18.02044	1353.657
2×10^7	1	π	512×193	18.14193	1371.593
2.4×10^7	1	π	512×193	19.04221	1507.890
2.8×10^7	1	π	512×193	19.83413	1633.418
$10^{30/4}$	1	π	512×193	20.47798	1739.647
4.5×10^7	1	π	512×193	22.44036	2087.182
$10^{31/4}$	1	π	512×193	23.76002	2340.822
10^8	1	π	768×257	27.50669	3144.931

$10^{33/4}$	1	π	768×257	31.81154	4220.616
2.15×10^8	1	π	768×257	33.36657	4649.541
$10^{34/4}$	1	π	768×257	36.75427	5658.648
4.64×10^8	1	π	896×321	40.44652	6875.704
$10^{35/4}$	1	π	896×321	42.42917	7580.057
10^9	1	π	1024×321	48.94284	10145.79
$10^{37/4}$	1	π	1024×321	56.42926	13571.10
2.15×10^9	1	π	1024×321	59.13988	14935.81
2.5×10^9	1	π	1024×321	61.38714	16116.94
$10^{38/4}$	1	π	1024×321	65.06338	18145.61
$10^{153/16}$	1	π	1024×321	67.42466	19511.79
4×10^9	1	π	1024×321	68.96487	20429.24
4.64×10^9	1	π	1024×321	71.58241	22019.93
$10^{39/4}$	1	π	1024×321	75.09725	24262.22
10^{10}	1	π	1024×321	86.68318	32430.06
$10^{41/4}$	1	π	1024×321	100.0909	43339.02
2×10^{10}	1	π	1024×321	103.0738	45995.60
2.15×10^{10}	1	π	1024×321	104.9517	47705.08

Table S1: Details for numerical solutions with $\text{Pr} = 1$ and $\Gamma = 2$. N_x and N_z represent the numbers of Fourier and Chebyshev modes, respectively.

-
- [1] L.-A. Couston, D. Lecoanet, B. Favier, and M. Le Bars, Phys. Rev. Research **2**, 023143 (2020).
- [2] X. Zhu, V. Mathai, R. J. Stevens, R. Verzicco, and D. Lohse, Physical Review Letters **120** (2018), 10.1103/physrevlett.120.144502.
- [3] M. Ossendrijver, Astronomy & Astrophysics Reviews **11**, 287 (2003).
- [4] W. V. R. Malkus, Proceedings of the Royal Society of London. Series A, Mathematical and Physical Sciences **225**, 196 (1954).
- [5] L. N. Howard, in *Applied Mechanics*, edited by H. Görtler (Springer Berlin Heidelberg, Berlin, Heidelberg, 1966) pp. 1109–1115.
- [6] R. H. Kraichnan, Physics of Fluids **5**, 1374 (1962).
- [7] E. A. Spiegel, Journal of Geophysical Research **67**, 3063 (1962).
- [8] B. Castaing, G. Gunaratne, L. Kadanoff, A. Libchaber, and F. Heslot, Journal of Fluid Mechanics **204**, 1 (1989).
- [9] S. GROSSMANN and D. LOHSE, Journal of Fluid Mechanics **407**, 27–56 (2000).
- [10] G. Ahlers, S. Grossmann, and D. Lohse, Rev. Mod. Phys. **81**, 503 (2009).
- [11] K. Julien and E. Knobloch, Journal of Mathematical Physics **48**, 065405 (2007).
- [12] K. Julien, E. Knobloch, A. M. Rubio, and G. M. Vasil, Phys. Rev. Lett. **109**, 254503 (2012).
- [13] F. Waleffe, A. Boonkasame, and L. Smith, Physics of Fluids **27**, 051702 (2015).
- [14] D. Sondak, L. M. Smith, and F. Waleffe, Journal of Fluid Mechanics **784**, 565 (2015), arXiv:1507.03151 [physics.flu-dyn].
- [15] B. Wen, D. Goluskin, and C. Doering, (2020).
- [16] G. P. Chini and S. Cox, Physics of Fluids **21**, 083603 (2009).
- [17] G. Yalnı, B. Hof, and N. Burak Budanur, arXiv e-prints, arXiv:2007.02584 (2020), arXiv:2007.02584 [physics.flu-dyn].
- [18] P. Cvitanović and J. Gibson, Physica Scripta **2010**, 014007 (2010).
- [19] J. B. Marston, G. P. Chini, and S. M. Tobias, Phys. Rev. Lett. **116**, 214501 (2016), arXiv:1601.06720 [physics.flu-dyn].
- [20] C. Beaume, G. P. Chini, K. Julien, and E. Knobloch, Physical Review E **91** (2015), 10.1103/phys-reve.91.043010.
- [21] G. Michel and G. P. Chini, Journal of Fluid Mechanics **858**, 536–564 (2019).
- [22] L. R. O. F.R.S., The London, Edinburgh, and Dublin Philosophical Magazine and Journal of Science **32**, 529 (1916).
- [23] K. J. Burns, G. M. Vasil, J. S. Oishi, D. Lecoanet, and B. P. Brown, Physical Review Research **2**, 023068 (2020), arXiv:1905.10388 [astro-ph.IM].
- [24] H. Johnston and C. R. Doering, Phys. Rev. Lett. **102**, 064501 (2009).
- [25] J. D. Scheel and J. Schumacher, Journal of Fluid Mechanics **802**, 147–173 (2016).
- [26] E. H. Anders, B. P. Brown, and J. S. Oishi, Phys. Rev. Fluids **3**, 083502 (2018).
- [27] R. Verzicco and R. Camussi, Physics of Fluids **9**, 1287 (1997), <https://doi.org/10.1063/1.869244>.
- [28] J. Boussinesq, (1877).
- [29] D. Lecoanet, M. McCourt, E. Quataert, K. Burns, G. Vasil, J. Oishi, B. Brown, J. Stone, and R. O’Leary, Monthly Notices of the Royal Astronomical Society **455**, 4274 (2016), publisher Copyright: © 2015 The Authors.
- [30] P. G. Drazin and W. H. Reid, *Hydrodynamic Stability*, 2nd ed., Cambridge Mathematical Library (Cambridge University Press, 2004).
- [31] S. B. Pope, *Turbulent Flows* (Cambridge University Press, 2000).

- [32] O. Shishkina, S. Horn, S. Wagner, and E. S. C. Ching, Phys. Rev. Lett. **114**, 114302 (2015).
- [33] X. Zhang, D. P. M. van Gils, S. Horn, M. Wedi, L. Zwirner, G. Ahlers, R. E. Ecke, S. Weiss, E. Bodenschatz, and O. Shishkina, Phys. Rev. Lett. **124**, 084505 (2020).